

L. Ma
J. J. K. Daemen

Strain rate dependent strength and stress–strain characteristics of a welded tuff

Received: 22 November 2004
Accepted: 5 November 2005
© Springer-Verlag 2006

Abstract Results of 61 uniaxial compression tests on the welded Topopah Spring tuff are presented. The tests were carried out under constant strain rates at room temperature. Stress–strain analysis indicates that dilatancy and compaction start at about 50% of ultimate strength. A sudden stress drop occurs at about 90% of the ultimate strength, which indicates the onset of specimen failure. Both strength and peak axial strain decrease with strain rate as power functions. Based on the strain rate dependence of strength and peak axial strain, it is inferred that the elastic modulus is strain rate dependent. A relationship between stress, axial strain, and axial strain rate is developed. The parameters in this relation are estimated using multivariate regression to fit stress–axial strain–strain rate data.

Keywords Strain rate dependence · Welded tuff · Dilatancy · Compaction

Résumé Les résultats de 61 essais de compression simple sur les

ignimbrites de Topopah Spring sont présentés. Les essais ont été réalisés avec une vitesse de déformation constante à la température du laboratoire. L'analyse en contrainte-déformation montre que la dilatance ou la contractance commence à environ 50% de la résistance ultime. Une chute brutale de résistance apparaît à environ 90% de la résistance ultime, ce qui rend compte de l'initiation de la rupture de l'échantillon. A la fois la résistance ultime et la déformation au pic de résistance diminuent avec la vitesse de déformation suivant des fonctions puissance. Sur la base de ces observations, il est conclu que le module d'élasticité dépend de la vitesse de déformation. Une relation entre contrainte, déformation axiale et vitesse de déformation axiale est mise en évidence. Les paramètres intervenant dans cette relation sont estimés à partir des techniques de régression linéaire sur les données expérimentales.

Mots clés Ignimbrites · Essais de compression simple · Paramètres mécaniques

L. Ma (✉)
Vector Engineering, Inc., 143E Spring Hill
Drive, Grass Valley, CA 95945, USA
E-mail: ma@vectoreng.com
Tel.: +1-530-2722448
Fax: +1-530-2728533

J. J. K. Daemen
Department of Mining Engineering,
University of Nevada, Reno,
NV 89557, USA

Introduction

Results of 61 uniaxial compression tests on welded Topopah Spring tuff are presented. The tests were carried out under constant strain rates at room temperature.

The purpose of the tests was to investigate the strain rate dependence of strength and stress–strain characteristics as a basis to investigate the long term mechanical behavior of the tuff. The tuff is from the welded Topopah Spring Formation at Yucca Mountain, Nevada.

Yucca Mountain has been selected as a candidate site for a High Level Nuclear Waste Repository in the United States (OCRWM 2004). The repository is to be excavated in the welded Topopah Spring tuff. Units exposed in the formation include the crystal-poor upper lithophysal zone (Ttptul), the crystal-poor middle nonlithophysal zone (Ttptmn), the crystal-poor lower lithophysal zone (Ttptll) and the crystal-poor lower nonlithophysal zone (Ttptln) (OCRWM 1999). The specimens tested were from Alcove#5, located in the middle nonlithophysal zone.

Lithophysae are gas-formed voids created soon after emplacement of the ash-flow tuff. Although they indicate a lithophysal zones some (usually small ones) also appear in the nonlithophysal zones. Vapor-phase altered spots (regions of tuff matrix altered by gases in the early stages of tuff emplacement, see OCRWM 1999; Buesch and Spengler 1998) are common in the welded Topopah Spring tuff.

The test specimens were prepared from nominal diameter 61 mm drill cores received from the sample management facility (SMF), Yucca Mountain Site Characterization Project. Although small vapor-phase altered spots were difficult to avoid, as far as possible the samples selected did not contain lithophysae or major vapor-phase altered spots. The specimens could not be cut to the same lengths due to the limitations of the length of the cores and the observed presence of lithophysae as well as major vapor-phase altered spots. However, the length to diameter ratio was controlled in the range of 1.8–2.9 to approximately meet ASTM D 4543 (ASTM 1991) and ISRM Suggested Method (ISRM 1979). As seen in Fig. 1, the strength of the specimens exhibited some length effect; with an apparent decrease in strength with the longer samples as indicated with best fit straight line. The figure also shows the strength of the tuff is highly variable.

The 61 specimens were divided into five groups to test at five strain rates. The specimens of various lengths were randomly grouped and it was assumed that in this

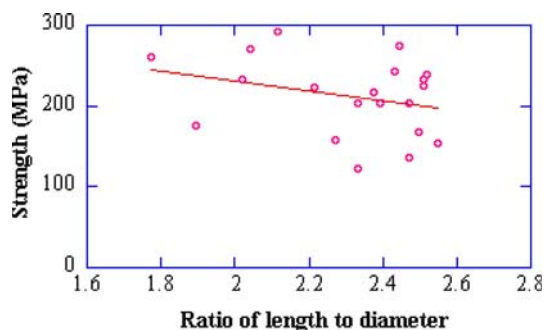


Fig. 1 Length effect on uniaxial compressive strength. Twenty tests at strain rates on the order of 10^{-5} s^{-1} are included

way the length effect among the groups would be cancelled out.

The moisture contents were measured for 58 of the 61 specimens. For the 41 for which the moisture content was determined before compression testing, the mean moisture content was 0.69% with a standard deviation of 0.1%. For 17 of the cores the moisture content was measured soon after testing; the mean moisture content and standard deviation were 0.75 and 0.07%. The porosity of the specimens in the welded Topopah Spring Formation is in the range of 10–13% according to Rautman and Engstrom (1996a, b), Engstrom and Rautman (1996) and DOE/RW-0549 (2002).

All the specimens exhibited brittle failure, at all strain rates. They failed violently, accompanied by intense noise, shock and dust. When a high strain rate test was performed the specimen usually broke into a large number of small pieces. The fractures were nearly parallel to the axis of the specimens, which failed predominantly by longitudinal splitting (Fig. 2). Previous investigations on deformation in brittle rocks have strongly suggested that the inelastic deformation and failure of brittle rocks under uniaxial compression is caused by the development of cracks parallel to the compressive stress direction (Walsh 1965; Brace et al. 1966; Cruden 1971; Lajtai 1971; Kranz and Scholz 1977; Horii and Nemat-Nasser 1985; Costin 1985; Lemaitre 1992; Ladanyi 1993; Martin 1997).

If a uniform stress is applied to a polycrystalline aggregate, the local stress at a point will not, in general, be the same as the applied stress but will vary in some complex way throughout the body (Scholz 1968). This inhomogeneity is the basic factor governing the microfracturing of a brittle rock (Costin and Holcomb 1983). As a rock approaches failure, cracks begin to interact and coalesce, finally forming macrocracks and faults (Lauterbach and Gross 1998).

Experimental setup and results

All the tests were conducted in a material testing system (MTS), servo-controlled hydraulic test system. Load was measured using a load cell. Displacement was measured using an linear variable differential transducer (LVDT) in the MTS. Strain was measured using electrical resistance strain gauges. Six strain gauges cemented at about mid-height on each specimen were used on each specimen, four measuring axial strain and two lateral strain. The strain in each direction was calculated by averaging all measurements in that direction. The five strain rates at which the specimens were tested were in the order of 10^{-4} , 10^{-5} , 10^{-6} , 10^{-7} and 10^{-8} s^{-1} . The test durations corresponding to each strain rate were about 1 min, 10 min, 1 day, 3 days and 7 days.

Fig. 2 Specimens after failure. Longitudinal splitting dominates the failure mode. Vapor-phase altered (*white*) spots are present inside the specimens: 01023668-3-U (strain rate = $1.36 \times 10^{-8} \text{ s}^{-1}$) and 01023657-1-U (strain rate = $1.13 \times 10^{-5} \text{ s}^{-1}$)



All the tests were performed using displacement control instead of true strain control. The displacement measurement included both the deformation of steel platens and spacers and the deformation of each contact pair of specimen platens, spacers and load cell. Consequently, the strain rate calculated from the strain measured by strain gauges on the specimen was not perfectly constant, especially at the beginning of loading. The strain rate used for the study was estimated using least square linear fit over the 50–90% portion of the axial strain in the axial strain–time curve. Figure 3 gives an example. Table 1 presents a summary of the experimental results.

Analysis and discussion

Threshold stress at half strength

Stress–strain curves mirror the mechanical behavior of rocks as the dominant factors for brittle rocks are the

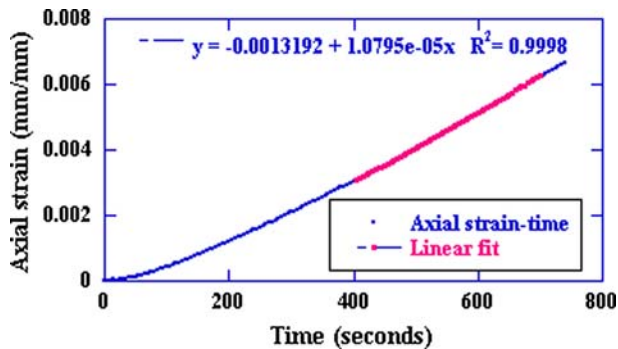


Fig. 3 Strain rate estimate using linear fit over 50–90% portion of axial strain–time curve (01023364-U, strain rate = $1.08 \times 10^{-5} \text{ s}^{-1}$)

microscopic activities, such as crack development and pore closure, which are reflected in the stress–strain curves (Bieniawski 1967). Figures 4, 5, and 6 give the stress–strain curves for three specimens, representing three different reversal modes of stress–crack volumetric strain curves observed in this study. Graph (a) in each figure shows axial stress versus axial strain, lateral strain, volumetric strain and crack volumetric strain. The axial and lateral strains are defined as positive for compression and negative for expansion. Assuming a small strain, volumetric strain is calculated by Eq. 1 according to Jaeger and Cook (1979, p. 84).

$$\varepsilon_v = \varepsilon + 2\varepsilon_l, \quad (1)$$

where ε is axial strain and ε_l is lateral strain. Graph (b) in each figure is the stress–crack volumetric strain curve with an enlarged scale along the horizontal axis. The three reversal modes of the stress–crack volumetric strain curves indicate three patterns of deformation, suggesting three types of microscopic activities occurred at the reversal points of the curves. The three patterns of deformation are dilatancy in Fig. 4, compaction in Fig. 5 and dilatancy followed by compaction in Fig. 6. The crack volumetric strain is defined as the difference between volumetric strain and elastic volumetric strain (Eberhardt et al. 1998; Lajtai 1998), and calculated by

$$\varepsilon_{cv} = \varepsilon_v - \varepsilon_{ev}, \quad (2)$$

where ε_{ev} = elastic volumetric strain, given by

$$\varepsilon_{ev} = (1 - 2\nu)/E \times \sigma, \quad (3)$$

where E and ν are Young's modulus and Poisson's ratio, respectively, σ is the axial stress. The crack volumetric strain measures the cumulative volume change of voids in a specimen. It inherits the sign convention of volumetric strain. For uniaxial compression, a negative value

Table 1 Summary of constant strain rate tests under uniaxial compression

Serial #	Specimen	Specimen length (mm)	Strain rate (s ⁻¹)	Strength (MPa)	Peak axial strain (mm/mm)
1	01023575-2-U	120	1.35E-07	101.80	0.0036
2	01023582-1-U	142	1.24E-05	202.98	0.0061
3	01023580-U	140	1.24E-06	172.00	0.0052
4	01023576-2-U	144	1.08E-07	128.59	0.0040
5	01023576-3-U	153	1.10E-08	163.28	0.0048
6	01023586-3-U	125	1.34E-08	253.29	0.0071
7	01023660-1-U	125	1.32E-07	168.10	0.0063
8	01023668-3-U	138	1.36E-08	113.21	0.0044
9	01023657-1-U	153	1.13E-05	233.16	0.0064
10	01023697-1-U	137	1.37E-07	215.19	0.0068
11	01023697-4-U	146	1.26E-07	163.16	0.0050
12	01023657-3-U	145	1.18E-05	216.95	0.0061
13	01023662-2-U	151	9.89E-06	203.36	0.0052
14	01023664-U	153	1.08E-05	239.62	0.0066
15	01023701-1-U	148	1.16E-05	242.89	0.0077
16	01023689-2-U	148	1.13E-04	228.02	0.0069
17	01023692-U	140	1.18E-04	213.68	0.0064
18	01023703-1-U	127	1.25E-04	264.53	0.0075
19	01025224-1-U	128	1.32E-04	209.32	0.0059
20	01023690-1-U	117	1.35E-04	248.61	0.0066
21	01025235-1-U	124	1.24E-04	285.88	0.0076
22	01025225-1-U	153	1.05E-04	196.68	0.0053
23	01025225-2-U	156	1.16E-04	217.53	0.0063
24	01023703-2-U	118	1.31E-04	214.41	0.0061
25	01023687-1-U	149	1.05E-05	275.22	0.0068
26	01023740-1-U	153	1.09E-05	225.33	0.0059
27	01025224-3-U	155	1.06E-05	154.49	0.0050
28	01025230-2-U	124	1.16E-05	269.62	0.0073
29	01023667-1-U	149	1.19E-06	176.63	0.0051
30	01025259-1-U	154	1.10E-06	238.26	0.0071
31	01025230-1-U	130	1.47E-06	209.46	0.0078
32	01023722-2-U	116	1.38E-06	296.47	0.0087
33	01025235-2-U	126	1.30E-06	229.75	0.0063
34	01023687-2-U	148	1.04E-06	213.02	0.0053
35	01023686-2-U	151	1.16E-06	242.43	0.0068
36	01023695-2-U	146	1.20E-05	203.02	0.0059
37	01025234-1-U	129	1.30E-05	291.64	0.0082
38	01023702-2-U	135	1.17E-05	223.90	0.0067
39	01023691-1-U	115	1.43E-06	259.94	0.0080
40	01023707-1-U	151	1.17E-06	192.01	0.0061
41	01023686-1-U	120	1.28E-06	232.54	0.0062
42	01025260-1-U	150	1.33E-06	212.17	0.0072
43	01023694-2-U	130	1.35E-06	244.80	0.0072
44	01023662-1-U	153	1.15E-07	204.55	0.0058
45	01025226-1-U	127	1.29E-07	227.37	0.0064
46	01025264-U	145	1.09E-07	119.22	0.0035
47	01023682-2-U	155	1.16E-07	121.15	0.0037
48	01023579-1-U	151	1.11E-05	135.97	0.0036
49	01023657-4-U	108	1.33E-05	261.63	0.0074
50	01023687-3-U	108	1.31E-07	241.02	0.0068
51	01023706-1-U	112	2.78E-08	199.89	0.0066
52	01023707-3-U	123	1.33E-05	232.55	0.0074
53	01023732-U	142	1.08E-05	122.28	0.0033
54	01023743-1-U	152	1.05E-05	167.47	0.0045
55	01023747-1-U	125	1.24E-06	264.26	0.0063
56	01023747-3-U	122	1.15E-04	210.88	0.0055
57	01023749-2-U	148	1.15E-06	157.6	0.0046
58	01023750-U	115	1.21E-05	176.52	0.0050
59	01023751-1-U	143	1.16E-07	176.95	0.0051
60	01023760-2-U	138	9.85E-05	158.24	0.0042
61	01025233-1-U	175	1.01E-07	197.48	0.0060

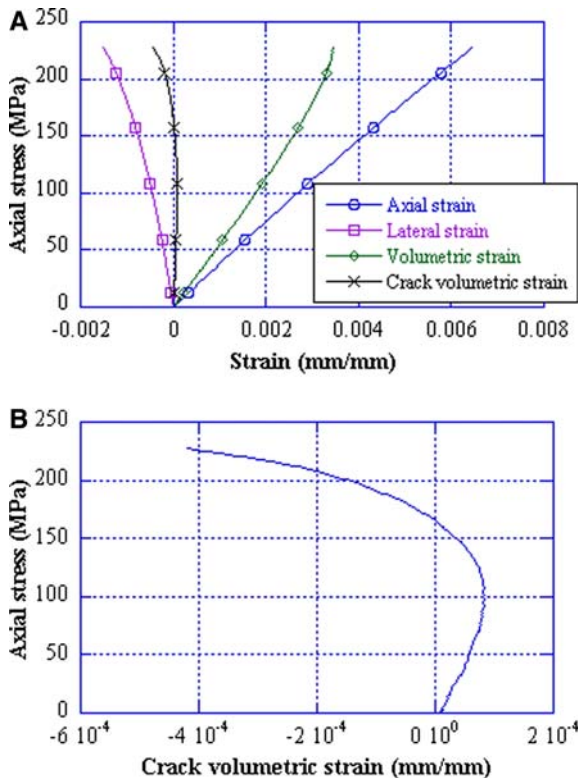


Fig. 4 Stress–strain curves for specimen 01025226-1-U (test duration = 15.3 h, strain rate = $1.29 \times 10^{-7} \text{ s}^{-1}$)

indicates dilatancy, which is caused by axial-oriented crack opening. A positive value indicates an opposite effect, i.e. compaction, according to Eq. 1, which can be the closure of pre-existing open voids (Lajtai 1998). The shape of the stress–crack volumetric strain curve actually reveals the interplay between these two distinct microscopic processes.

Dilatancy is an inelastic increase in volume due to stress. It is critical for brittle failure of rocks (Brace 1978). Lac du Bonnet granite (Martin and Chandler 1994; Lajtai 1998), Westerly granite (Holcomb 1981) and calcite marble (Brace et al. 1966) displayed obvious dilatancy with the growth of cracks parallel to the loading direction. If the magnitude of the dilatancy is sufficiently high, it can be observed in the stress–lateral strain curve as the curve deviates from the linear trend, and in the stress–volumetric strain curve as the curve reverses towards the negative direction.

Compaction of a specimen can be caused by pore closure under axial loading. Vajdova et al. (2004) proposed that compressibility and porosity are positively correlated. For a low to moderately stiff rock matrix, the pores would close at low stress. Thus the pore closure is usually indicated in the lower portion of a stress–axial strain curve by exhibiting upward convex curvature (Bieniawski 1967). In Figs. 4, 5 and 6 the near linearity of the lower half parts of the stress–axial strain curves

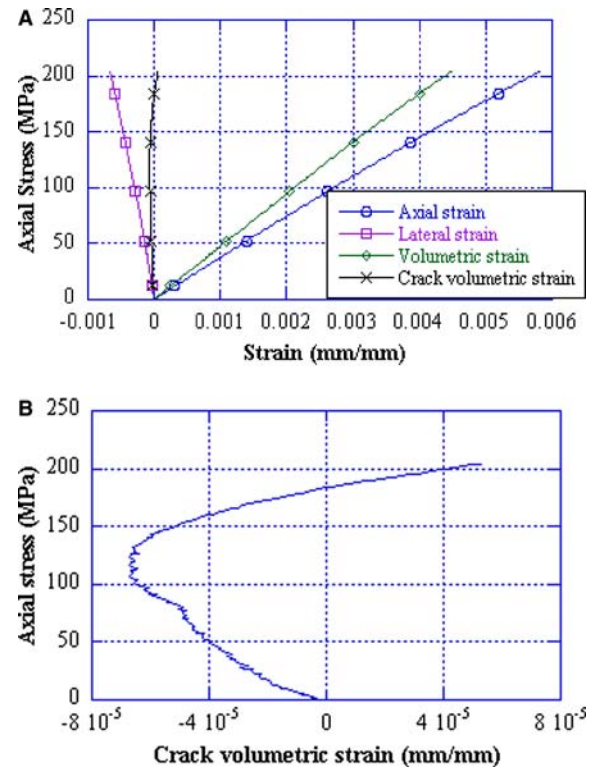


Fig. 5 Stress–strain curves for specimen 01023662-1-U (test duration = 15.8 h, strain rate = $1.15 \times 10^{-7} \text{ s}^{-1}$)

indicates that the matrices of the specimens are quite stiff given the porosity range of 10–13% for the welded Topopah Spring tuff.

In Figs. 4, 5 and 6, the stress–axial strain curves become slightly more nonlinear at about half the peak stresses, with downward bending. As the stresses increase further, the curves depart from linearity faster.

For specimen 01025226-1-U in Fig. 4 the stress–crack volumetric curve is initially positive. It goes through a reversal point (108 MPa) and ends with a negative value (indicating dilatancy). From the viewpoints of Martin and Chandler (1994) and Eberhardt et al. (1998), the reversal point is where the axial-oriented cracks start to initiate.

Compared with specimen 01025226-1-U, the stress versus crack volumetric strain curve of specimen 01023662-1-U in Fig. 5 changes in the opposite direction (indicating compaction). The reversal point is at about 115 MPa. To achieve this opposite reversal, a relatively large axial deformation must develop.

Figure 6 shows a combined case in which the stress–crack volumetric strain curve reverses twice, indicating dilatancy followed by compaction. The first reversal point is at about 120 MPa. The second one is at about 225 MPa, 92% of the strength of the specimen. The second reversal point may indicate the onset of failure, because a significantly larger deformation in the axial

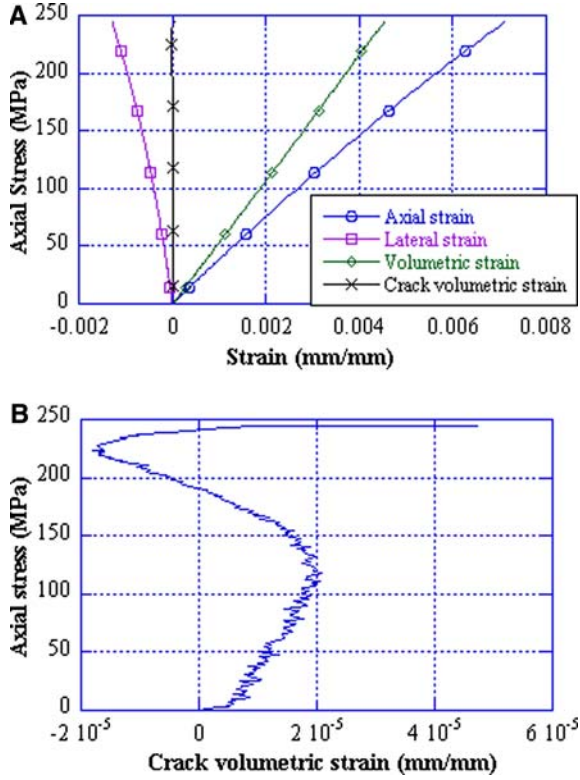


Fig. 6 Stress–strain curves for specimen 01023694-2-U (test duration = 1.7 h, strain rate = $1.35 \times 10^{-6} \text{ s}^{-1}$)

direction starts to develop. If this is true, then the rock matrix has started breaking at this stress.

Reversal points were observed in the stress versus crack volumetric strain curves for 15 of the 61 tests. The reversal stress levels and the reversal directions for these tests are summarized in Table 2. The ratio of reversal stress to strength for each test is also listed. This ratio does not change significantly from test to test. Its mean value is 52% with the standard deviation 9%.

Table 2 Summary of reversal stresses for 15 tests

Specimen	Reversal stress (MPa)	Strength (MPa)	Reversal stress / Strength	Reversal direction	Strain rate
01023580-U	105	172.00	0.61	+ to -	1.24E-06
01023662-2-U	105	203.36	0.52	- to +	9.89E-06
01025224-1-U	102	209.32	0.49	- to +	1.32E-04
01025225-2-U	80	217.53	0.37	- to +	1.16E-04
01025224-3-U	80	154.49	0.52	- to +	1.06E-05
01025230-2-U	140	269.62	0.52	- to +	1.16E-05
01025259-1-U	175	238.26	0.73	- to +	1.10E-06
01025230-1-U	120	209.46	0.57	- to +	1.47E-06
01023694-2-U	120	244.80	0.49	+ to -	1.35E-06
01023662-1-U	115	204.55	0.56	- to +	1.15E-07
01025226-1-U	105	227.37	0.46	+ to -	1.29E-07
01023706-1-U	115	199.89	0.58	- to +	2.78E-08
01023751-1-U	60	176.95	0.34	+ to -	1.16E-07
01023695-2-U	105	203.02	0.52	- to +	1.20E-05
01023760-2-U	80	158.24	0.51	+ to -	9.85E-05

“+ to -” indicates dilatancy;
“- to +” indicates compaction

In Table 2, 5 of the 15 tests exhibited dilatancy inferring initiation of axial-oriented cracks while the remaining 10 exhibited compaction, suggesting pore closure. These two microscopic activities took place almost simultaneously. At a given porosity, which of these phenomena appeared first depended mainly on the strength of the specimen. The following statistical study suggests that specimens with higher strength show compaction, i.e. pore closure, occurring first. A multivariate regression model can be built as

$$D_{\text{Rev}} = \beta_0 + \beta_1 \times \sigma_{\text{peak}} + \beta_2 \times \log \dot{\epsilon} + e, \quad (4)$$

where D_{Rev} represents reversal direction, a binary variable, set to 0 for dilatancy, 1 for compaction; σ_{peak} is the peak stress or ultimate uniaxial compressive strength of a specimen; $\log \dot{\epsilon}$ is the logarithm of strain rate; β_0 is the intercept in the model; β_1 and β_2 are coefficients of the independent variables; e is the error term. Regressing D_{Rev} on σ_{peak} and $\log \dot{\epsilon}$, the intercept and coefficients are estimated as in Eq. 5. The P values for student t tests are 0.39 for σ_{peak} and 0.41 for $\log \dot{\epsilon}$.

$$D_{\text{Rev}} = 0.434 + 0.004\sigma_{\text{peak}} + 0.097 \log \dot{\epsilon}. \quad (5)$$

In Eq. 5, D_{Rev} increases (towards 1) with an increase of σ_{peak} and an increase of $\log \dot{\epsilon}$. This means that a high strength and a high strain rate contribute to compaction (coded 1), while a low strength and a low strain rate contribute to dilatancy (coded 0). This regression study suggests that a high strength makes a specimen close its pores prior to dilatancy. It also suggests that dilatancy of a specimen tends to develop prior to compaction with a decrease of strain rate.

Threshold stress at near failure

To explore the near failure behavior of the tuff specimens, stress–axial strain curves for all the 61 tests have

been plotted and examined. A clear stress drop in the stress–axial strain curve near failure was observed in 25 tests. Figure 7 illustrates four of them. Table 3 summarizes the stresses at the drop points in the stress–axial strain curves near failure for the 25 tests.

The mean value for the ratio of stress at drop point to strength can be interpreted to indicate that on average when the axial stress reaches 93.8% ultimate uniaxial compressive strength, a sudden stress drop or a sudden axial deformation occurs. This is an indication of onset of specimen failure. It may be the start of crack interaction according to Lauterbach and Gross (1998). The stress at drop point may have a similar significance as the second reversal point in Fig. 6.

Strain rate dependence of strength and peak axial strain

The strength and peak axial strain (ϵ_{peak}) for the 61 tests have been determined. Plots for strength and peak axial strain as functions of strain rate, in semi-log scale, are shown in Figs. 8 and 9. Nonlinear regression was applied to estimate the relations between strength and axial strain rate and between peak axial strain and strain rate. The regression was conducted using PROC NLIN with Marquardt algorithm in SAS (Version 8.2) program (Fernandez 2003). The PROC NLIN is a procedure to

Table 3 Near failure stresses at drop points in stress–axial strain curve for 25 tests

Specimen	Stress at drop point (MPa)	Strength (MPa)	$\frac{\text{Stress at drop point}}{\text{Strength}}$
01023582-1-U	184.99	202.98	0.91
01023580-U	164.33	172.00	0.96
01023576-2-U	114.83	128.59	0.89
01023668-3-U	101.67	113.21	0.90
01023697-1-U	206.58	215.19	0.96
01023662-2-U	189.79	203.36	0.93
01023689-2-U	215.03	228.02	0.94
01023692-U	205.36	213.68	0.96
01023690-1-U	224.58	248.61	0.90
01025225-1-U	188.16	196.68	0.96
01023703-2-U	206.06	214.41	0.96
01025259-1-U	225.84	238.26	0.95
01023722-2-U	288.32	296.47	0.97
01025234-1-U	277.34	291.64	0.95
01023702-2-U	212.41	223.90	0.95
01023707-1-U	171.55	192.01	0.89
01025260-1-U	194.81	212.17	0.92
01023682-2-U	112.79	121.15	0.93
01023706-1-U	189.38	199.89	0.95
01023707-3-U	220.73	232.55	0.95
01023747-1-U	250.89	264.26	0.95
01023747-3-U	199.96	210.88	0.95
01023750-U	163.25	176.52	0.92
01023760-2-U	145.68	158.24	0.92
01025233-1-U	192.56	197.48	0.98

$\frac{\text{Stress at drop point}}{\text{Strength}}$: mean = 93.8%, standard deviation = 2.4%

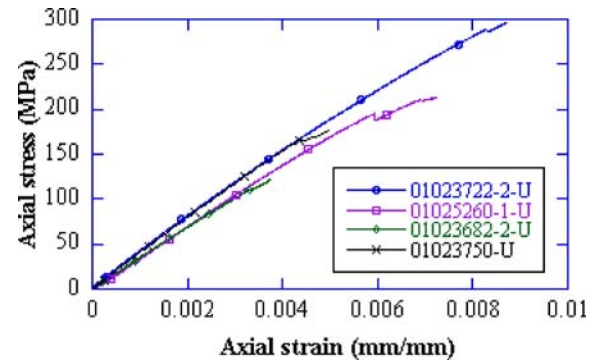


Fig. 7 Stress–axial strain curves showing stress drop before failure. Specimen 01023722-2-U: strength = 296.47 MPa, strain rate = $1.23 \times 10^{-6} \text{ s}^{-1}$; Specimen 01025260-1-U: strength = 212.17 MPa, strain rate = $1.18 \times 10^{-6} \text{ s}^{-1}$; Specimen 01023682-2-U: strength = 121.15 MPa, strain rate = $1.02 \times 10^{-7} \text{ s}^{-1}$; Specimen 01023750-U: strength = 176.52 MPa, strain rate = $1.15 \times 10^{-5} \text{ s}^{-1}$

find least squares estimates of coefficients for nonlinear models. The Marquardt algorithm is a direct numerical search method. The relations of strength–strain rate and peak axial strain–strain rate are best represented by power functions, as given in Eqs. 6 and 7. Regression curves and the 95% confidence bands for the relations are added in Figs. 8 and 9.

$$\sigma_{\text{peak}} = 297.8\dot{\epsilon}^{0.028}, \quad (6)$$

$$\epsilon_{\text{peak}} = 0.0074\dot{\epsilon}^{0.016}. \quad (7)$$

Student's *t* test indicates that the exponent in Eq. 6 is significantly different from zero at the 95% confidence level (*P* value = 0.0087, less than 0.05), but the exponent in Eq. 7 is not (*P* value = 0.12, greater than 0.05).

Both strength and peak axial strain decrease with strain rate following power functions. Analyses indicate that the sensitivity of strength to strain rate is higher than the sensitivity of peak axial strain to strain rate. The difference is accounted for by the ratio of strength to peak axial strain (Ma 2004; Ma and Daemen 2004). This ratio defines the secant elastic modulus at failure (Jaeger and Cook 1979, p. 79). Thus the secant elastic modulus decreases with strain rate.

Strain rate dependent stress–strain relation

All the specimens exhibited some nonlinear deformation. This nonlinearity becomes slightly clearer after about mid strength. The inelasticity of the specimens was very small compared with their elasticity (Ma and Daemen 2004). The stress can be expressed as a function of axial strain for Cauchy elastic materials (Desai and Siriwardane 1994, p. 83). For a given strain rate, the derivative of stress with respect to axial strain gives the

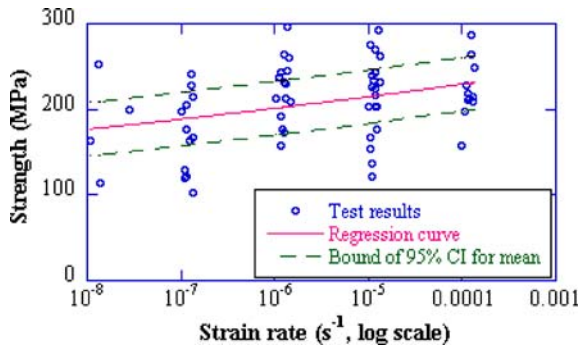


Fig. 8 Strength as a power function of strain rate with regression line and 95% confidence bands

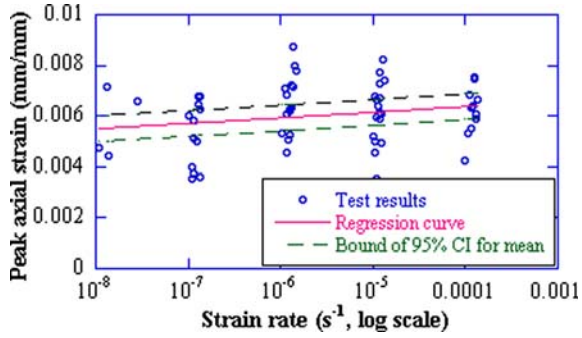


Fig. 9 Peak axial strain as a power function of strain rate with regression line and 95% confidence bands

tangent elastic modulus as in Eq. 8 (Jaeger and Cook 1979, p. 79).

$$E = \frac{d\sigma}{d\varepsilon}. \quad (8)$$

From the previous section, the secant elastic modulus depends on strain rate. This is also true for the tangent elastic modulus. Taking the derivative of E in Eq. 8 with respect to $\dot{\varepsilon}$

$$\frac{dE}{d\dot{\varepsilon}} = \frac{\partial^2 \sigma}{\partial \varepsilon \partial \dot{\varepsilon}}. \quad (9)$$

The right hand side of Eq. 9 can be written as

$$\frac{\partial^2 \sigma}{\partial \varepsilon \partial \dot{\varepsilon}} = f(\varepsilon, \dot{\varepsilon}). \quad (10)$$

The relationship of stress and axial strain for non-linear elastic rocks under a fixed strain rate can be written as in Eq. 11 (Zheng 1988, p. 216)

$$\sigma = A\varepsilon^l, \quad (11)$$

where A and l are material constants. The parameter l is often called the strain hardening exponent. A is termed the strain-hardening coefficient.

For a constant axial strain, the relationship of stress and strain rate must agree with the form in Eq. 6, which can be expressed as

$$\sigma = B\dot{\varepsilon}^k \quad (12)$$

where B and k are material constants.

Both relations of stress–axial strain and stress–strain rate are given as power functions. Integrating Eq. 10 for σ and applying initial conditions, the relation of stress, axial strain and strain rate can be obtained as

$$\sigma = C\varepsilon^m \dot{\varepsilon}^n, \quad (13)$$

where C , m and n are material constants.

Compiling the stress–axial strain–strain rate data for the 61 tests and letting Eq. 13 fit the data using multivariate regression with logarithmic transformation, Eq. 14 is obtained, which gives a good description of the relationship between the three variables by giving the R^2 as 0.98.

$$\sigma = 39670\varepsilon^{0.955}\dot{\varepsilon}^{0.026} \quad (14)$$

Equation 14 gives the general trend of how stress varies with axial strain and strain rate for the welded Topopah Spring tuff from the nonlithophysal zone (Ttptmn). Figure 10 is a cluster of stress–axial strain curves for five strain rates. It is constructed based on Eq. 14 in conjunction with Eq. 7, because Eq. 7 gives the restriction of peak axial strain decreasing with strain rate.

Conclusions

- Two threshold stresses were observed in stress–strain curves: the first one, at about mid strength, suggests the start of crack initiation and pore closure; the second, a stress drop near failure, indicates the onset of specimen failure. The second threshold stress may be the start of crack interaction. More nonlinear

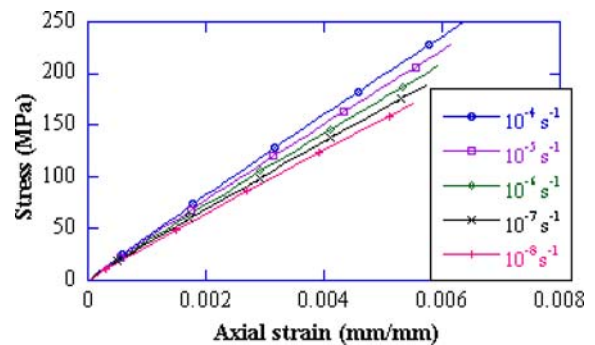


Fig. 10 Stress as a function of axial strain and strain rate

deformation is generated between these two threshold stresses. In future studies and in engineering application, more attention should be paid to this stress range. As pointed out by Hoek and Brown (1980, p. 150), the use of the conventionally defined uniaxial compressive strength (i.e., as measured in a 10–15 min test) may not be the most appropriate definition of strength.

2. Both strength and peak axial strain decrease as power functions of strain rate. Strength is more sensitive to strain rate than is peak axial strain, which implies that the elastic modulus is strain rate dependent.
3. A multiplication form of a power function of axial strain and a power function of strain rate is a good expression of stress under the condition of axial strain and strain rate variation. This establishes an empirical relation between stress, axial strain and strain rate.

Acknowledgements The authors thank Mr. Jaime Gonzalez, DOE Contract Manager, Mr. Rick Blitz for experimental work and for valuable discussions and Dr. Mark Board for most helpful discussions and suggestions. This paper was prepared by the University of Nevada Reno pursuant to a Cooperative Agreement fully funded by the United States Department of Energy, and neither University and Community College System of Nevada nor any of its contractors or subcontractors nor the United States Department of Energy, nor any person acting on behalf of either: (a) Makes any warranty or representation, express or implied, with respect to the accuracy, completeness, or usefulness of the information contained in this report, or that the use of any information, apparatus, method, or process disclosed in this report may not infringe privately-owned rights; or (b) Assumes any liabilities with respect to the use of, or for damages resulting from the use of, any information, apparatus, method or process disclosed in this report. Reference herein to any specific commercial product, process, or service by trade name, trademark, manufacturer, or otherwise, does not necessarily constitute or imply its endorsement, recommendation, or favoring by the United States Department of Energy. The views and opinions of authors expressed herein do not necessarily state or reflect those of the United States Department of Energy.

References

- ASTM (American Society for Testing and Materials D 4543–85) (Reapproved 1991) Standard practice for preparing rock core specimens and determining dimensional and shape tolerances. Annual Book of ASTM Standards, Section 4, Construction, Vol 04.08 Soil and Rock; Building Stones. Conshohocken, PA
- Bieniawski ZT (1967) Mechanism of brittle fracture of rock: Part I-theory of the fracture process. *Int J Rock Mech Min Sci* 4:395–406
- Brace WF (1978) Volume changes during fracture and frictional sliding: a review. *Pure Appl Geophys* 116:603–614
- Brace WF, Paulding BW Jr and Scholz CH (1966) Dilatancy in the fracture of crystalline rocks. *J Geophys Res* 71:3939–3953
- Buesch DC, Spengler RW (1998) Character of the middle nonlithophysal zone of the Topopah Spring Tuff at Yucca Mountain. In: High-level radioactive waste management. Proceedings of the Eighth International Conference, Las Vegas, Nevada
- Costin LS (1985) Time-dependent damage and creep of brittle rock. In: Stubbs N, Krajcinovic D (eds) Damage mechanics and continuum modeling. Proceedings of 2 Sessions Sponsored by the Engineering Mechanics Division of the American Society of Civil Engineers in Conjunction with the ASCE Convention, Detroit, Michigan
- Costin LS, Holcomb DJ (1983) A continuum model of inelasticity deformed brittle rock based on the mechanics of microcracks. In: Desai CS, Gallagher RH (eds) Constitutive laws for engineering materials theory and application. Proceedings of the International Conference. Tucson, Arizona, USA
- Cruden DM (1971) The form of the creep law for rock under uniaxial compression. *Int J Rock Mech Min Sci* 8:105–126
- Desai CS, Siriwardane HJ (1994) Constitutive laws for engineering materials with emphasis on geologic materials. Prentice-Hall, Englewood Cliffs
- DOE/RW-0549 (2002) Yucca Mountain site suitability evaluation. DOE report. Website: http://www.yucca-we-b2.ymp.gov/documents/sse_a
- Eberhardt E, Stead D, Stimpson B and Read RS (1998) Identifying crack initiation and propagation threshold in brittle rock. *Can Geotech J* 35:222–233
- Engstrom DA, Rautman CA (1996) Geology of the USW SD-9, Drill Hole Yucca Mountain, Nevada. Sandia Report, SAND96–2030, UC-814, Sandia National Laboratories
- Fernandez G (2003) Data mining using SAS applications. Chapman and Hall/CRC, London/USA
- Hoek E, Brown ET (1980) Underground excavations in rock. Institution of Mining and Metallurgy, London
- Holcomb DJ (1981) Memory, relaxation, and microfracturing in dilatant rock. *J Geophys Res* 86:6235–6248
- Horii H, Nemat-Nasser S (1985) Compression-induced microcrack growth in brittle solids: axial splitting and shear failure. *J Geophys Res* 90:3105–3125
- ISRM (1979) Suggested method for determination of the uniaxial compressive strength of rock materials. *Int J Rock Mech Min Sci Geomech Abstr* 16:137–140
- Jaeger JC and Cook NGW (1979) Fundamentals of rock mechanics, 3rd edn. Chapman and Hall, London
- Kranz RL, Scholz CH (1977) Critical dilatant volume of rocks at the onset of tertiary creep. *J Geophys Res* 82:4893–4898
- Ladanyi B (1993) Time-dependent response of rock around tunnels. In: Hudson JA (ed) Comprehensive rock engineering, principles, practice and projects. Pergamon, Oxford 3:77–112
- Lajtai EZ (1971) A theoretical and experimental evaluation of the Griffith theory of brittle fracture. *Tectonophysics* 11:129–156
- Lajtai EZ (1998) Microscopic fracture processes in a granite. *Rock Mech Rock Eng* 31:237–250
- Lauterbach B and Gross D (1998) Crack growth in brittle solids under compression. *Mech Materials* 29:81–92
- Lemaitre J (1992) A course on damage mechanics. Springer, Berlin Heidelberg New York

- Ma L (2004) Experimental investigation of time dependent behavior of Welded Topopah Spring Tuff. Dissertation, University of Nevada, Reno
- Ma L, Daemen JJK (2004) Strain rate-dependence of mechanical properties of Welded Topopah Spring Tuff. *Int J Rock Mech Min Sci*, 41:395 (Spec Issu)
- Martin CD, Chandler NA (1994) The progressive fracture of Lac du Bonnet Granite. *Int J Rock Mech Min Sci Geomech Abstr* 31:643–659
- Martin RJ, Noel JS, Boyd PJ, Price RH (1997) Creep properties of the Paintbrush Tuff recovered from Borehole USW NRG-7/7A: Data report. SAND95–1759, UC-814, Sandia National Laboratories
- OCRWM (2004) Website: <http://www.ocrwm.doe.gov>
- OCRWM (Office of Civilian Radioactive Waste Management) (1999) Geology of the ECRB Cross Drift—exploratory studies facility, Yucca Mountain Project, Yucca Mountain, Nevada, prepared by Mongano GS, Singleton WL, Moyer TC, Beason SC, Eatman GLW, Albin AL, and Lung RC, Bureau of Reclamation and U.S. Geological Survey. Denver, Colorado
- Rautman CA, Engstrom DA (1996a) Geology of the USW SD-12 Drill Hole Yucca Mountain, Nevada. Sandia Report, SAND96-1368, UC-814, Sandia National Laboratories
- Rautman CA, Engstrom DA (1996b) Geology of the USW SD-7, Drill Hole Yucca Mountain, Nevada. Sandia Report, SAND96-1474, UC-814, Sandia National Laboratories
- Scholz CH (1968) Experimental study of the fracturing process in brittle rock. *J Geophys Res* 73:1447–1454
- Vajdova V, Braud P, Wong T (2004) Compaction, dilatancy, and failure in porous carbonate rocks. *J Geophys Res* 109 (B5)
- Walsh JB (1965) The effect of cracks on the uniaxial elastic compression of rocks. *J Geophys Res* 70:399–411
- Zheng Y (1988) Theoretical foundations of elasticity, plasticity and viscosity for rock mechanics (in Chinese). Coal Industry Press, Beijing